

Galaxy mergers classification using CNNs trained on Sérsic models, residuals and raw images.

D. Chudy¹, W. J. Pearson², A. Pollo^{2,1}, L. E. Suelves^{2,3}, B. Margalef-Bentabol⁴, L. Wang⁴, V. Rodriguez-Gomez⁵, and A. La Marca⁴

¹ Astronomical Observatory of the Jagiellonian University, Faculty of Physics, Astronomy and Applied Computer Science, ul. Orla 171, 30-244 Kraków, Poland

e-mail: dawid.chudy@doctoral.uj.edu.pl

² National Centre for Nuclear Research, Pasteura 7, 02-093 Warszawa, Poland

³ Tartu Observatory, University of Tartu, Observatooriumi 1, Tõravere 61602, Estonia

⁴ SRON Netherlands Institute for Space Research, Landleven 12, 9747 AD Groningen, The Netherlands

⁵ Instituto de Radioastronomía y Astrofísica, Universidad Nacional Autónoma de México, Apdo. Postal 72-3, 58089 Morelia, Mexico

Received MDY; accepted MDY

ABSTRACT

Context. Galaxy mergers are crucial for understanding galaxy evolution, and with large upcoming datasets, automated methods, such as Convolutional Neural Networks (CNNs), are needed for efficient detection. It is understood that these networks work by identifying deviations from the regular, expected shapes of galaxies, which are indicative of a merger event.

Aims. Using images from the IllustrisTNG simulations, we aim to check the importance of faint features, source position and shape information present in galaxy merger images on the performance of a CNN merger vs. non-merger classifier.

Methods. We fit Sérsic profiles to each galaxy in mock images from the IllustrisTNG simulations. We subtract the profiles from the original images to create residual images, and we train three identical CNNs on three different datasets – original images (CNN1), model images (CNN2), and residual images (CNN3).

Results. We found that it is possible to conduct galaxy merger classification based only on faint features, source position and shape information present in residual images and model images, respectively. The results show that the CNN1 correctly classifies 74% of images, while CNN2 70%, and CNN3 68%.

Conclusions. Source position and shape information is crucial for pre-merger classification, while residual features are important for post-merger classification. CNN3 classifies post-mergers in the latest merger stage the best out of all three classifiers.

Key words. Galaxies: merger – Galaxies: faint structures – Methods: machine learning – Techniques: image processing – Techniques: Sérsic profile fitting

1. Introduction

In the Lambda-cold dark matter cosmology, dark matter (DM) halos form due to gravitational instability, allowing baryonic matter to cool, accumulate, and form galaxies. These galaxies then grow through both accretion within these halos and mergers. Hence galaxy mergers provide crucial insights into how galaxies evolve over time. The merging process proceeds differently depending on the properties of colliding galaxies. Major mergers, where the stellar mass ratio of the merging components is up to 4:1, can combine their structures, resulting in a significant change in morphology if the components collide at the right speed and angle (Bournaud et al. 2005; Lotz et al. 2010). Conspicuous merger features, such as bridges, double nuclei, and tidal features (tails and plumes) of different sizes and shapes may appear (Toomre & Toomre 1972). This process can feed supermassive black holes, activating galactic nucleus (AGN) activities (Gao et al. 2020; Di Matteo et al. 2005), and trigger star formation (Pearson et al. 2019a; Ellison et al. 2013). When the mass of one of the merging galaxies is significantly larger than the mass of the other one (minor mergers), the merging process is less violent, and the less massive galaxy is usually incorporated into the larger one, leaving the larger galaxy fairly undisturbed.

The galaxy merger fraction has evolved significantly during cosmic time. It is believed that mergers account for less than 10% of the low-redshift galaxies (Ferreira et al. 2020; Mundy et al. 2017; Duncan et al. 2019), with the percentage increasing to 20% within $z \in [2, 3]$ (Tasca et al. 2014). The merger fraction decreases to 5% at $z \approx 6$ (Ventou et al. 2019). Merger rates in Illustris (Vogelsberger et al. 2014) simulations align with observational rates for medium-sized galaxies (Rodriguez-Gomez et al. 2015), therefore, the merger fraction in Illustris agrees with the merger fraction in observations.

It is possible to use visual inspection (Darg et al. 2010) to identify a merger, though this method is challenging to replicate consistently, time-consuming for large samples of galaxies, and may suffer from low accuracy, incompleteness (Huertas-Company et al. 2015), and human biases (Lambrides et al. 2021). Using morphological parameters is a way to quantify morphology with reliable and reproducible measurements. Concentration (Okamura et al. 1984; Kent 1985; Conselice 2003), Asymmetry (Conselice et al. 2000), and Smoothness (Takamiya 1999; Conselice 2003) (CAS parameters) and the bulge-merger statistics – a combination of the Gini coefficient (Abraham et al. 2003) and M_{20} (the second-order moment of the brightest 20% of the galaxy) (Lotz et al. 2004) – serve as feature detectors and are

often used for merger classification (Okamura et al. 1984; Abraham et al. 1996; Bershadsky et al. 2000; Snyder et al. 2015). Deriving those parameters requires images with sufficiently high spatial resolution. Conselice et al. (2000) has shown that the accuracy of CAS parameters begins to decline below the threshold value of 1 kpc pixel^{-1} . Another commonly used method to identify mergers is the close pair method, which selects galaxy pairs that are close on the sky and in redshift (Barton et al. 2000; Alonso et al. 2004; De Propris et al. 2005; Duncan et al. 2019). This method can use both spectroscopic and photometric observations (Lin et al. 2008). While spectroscopic methods provide greater precision than photometric techniques (Hildebrandt et al. 2008), they are also more resource-intensive. Identifying galaxy mergers may also be possible using only photometric information. Suelves et al. (2023) found that photometric bands, colours, and their errors provide accurate classification of SDSS observations.

With the advent of upcoming surveys such as *Euclid* (Lauferijs et al. 2011) and Legacy Survey of Space and Time (LSST; Ivezić et al. 2019) that will collect large amount of data it becomes even more important to create algorithms to automate time-consuming, repetitive tasks such as identifying galaxy mergers. The application of machine learning (ML) in the field of astronomy has experienced a significant surge over the past few years. Recent studies have shown that it is possible to use Convolutional Neural Networks (CNN) to address the visual merger classification problem. Ackermann et al. (2018) used transfer learning to fine-tune CNN trained to classify real life objects, using SDSS observations. Pearson et al. (2019b) trained one CNN with observations from SDSS and another with simulated galaxies from EAGLE observations receiving an accuracy of 91.5% and 65.2% respectively. Combination of CNNs and Linear Networks has led to creation of the North Ecliptic Pole merging galaxy catalogue (Pearson et al. 2022) for $z < 0.3$. Ćiprijanović et al. (2020) used a CNN to distinguish between mergers and non-mergers in simulated images from Illustris-1 at $z = 2$ with 79% accuracy. Bickley et al. (2021) showed that CNNs outperform Gini-M20 and asymmetry methods in post-merger and isolated galaxy classification. The performance of these networks vary due to many factors, including differences in setup. Margalef-Bentabol et al. (2024) conducted a systematic and consistent study between machine learning-based detection methods to understand the relative performance of different ML methods using the same training and test data. A total of six ML methods have been tested, based on the same mock IllustrisTNG simulation images generated to mimic the HSC data. All CNNs that were not pre-trained with other galaxy images show similar results, using different architectures. This may indicate that preprocessing the training data is a more important factor compared to the choice of parameters of the CNNs. The above works do not exhaust the issue of classifying mergers with CNNs and there are also other works on this topic. (e.g. Walmsley et al. 2019; Wang et al. 2020; Ferreira et al. 2020; Nevin et al. 2019; Sánchez et al. 2023)

The previous work on creating a CNN classifier for classifying merger galaxies relied on image preprocessing limited to augmentation and normalization (Ackermann et al. 2018; Pearson et al. 2019b, 2022; Ćiprijanović et al. 2020; Bickley et al. 2021). The wide range of characteristic features of mergers and their irregularity, especially subtle peculiarities, may cause these features to be inadequately captured by the network or get mixed up with other galaxy structures. Mantha et al. (2019) explored the use of Sérsic profile subtraction to extract merging features.

They developed a tool that extracts and quantifies residual substructures hosted by galaxies. This tool can help to clarify how merger signatures are identified, could enhance efforts to connect observed galaxy morphology to the underlying physical processes of merging, and improve merger detection techniques.

In this work, we create model images for each galaxy using Sérsic profile fits applied to every image. We then subtract these model images from the originals to produce the residual images. This process leaves behind everything that does not match the profile, possibly emphasizing faint merger peculiarities such as diffuse structures or tidal features. It is believed that they are of great importance for the classification (Pearson et al. 2022), so we want to explore whether CNNs can be trained on these faint structures. This work aims to test and compare the performance of CNNs trained on original and processed data, especially to check if it is possible to conduct galaxy merger classification based only on distorted structures present in the residual images. We trained three separate CNNs:

- CNN 1, trained on original images,
- CNN 2, trained on Sérsic profile images,
- CNN 3, trained on residual images.

This paper is structured as follows. In Sect. 2 we present the IllustrisTNG simulations data. In Sect. 3 we describe the data preprocessing, the models' architecture, and define performance metrics used for evaluation. In Sect. 4 we present performance of the models and study the models behaviour. In Sect. 5 we compare the performance of the models in merger classification task. In Sect. 6, we present our conclusions and future work. We assume a cosmology consistent with the Planck Collaboration et al. (2016) results ($\Omega_{\Lambda,0} = 0.6911$, $\Omega_{m,0} = 0.3089$, $h = 0.677$).

2. Data

2.1. Illustris TNG

Images used for this study come from Next Generation Illustris Simulations (IllustrisTNG, or TNG; Nelson et al. 2019), a cosmological gravo-magnetohydrodynamical simulations of formation and evolution of galaxies assuming cosmological parameters consistent with Planck Collaboration et al. (2016). TNG comprises of three runs, TN50 TNG100, and TNG300, with comoving box sizes of 50, 100, and 300 $\text{Mpc } h^{-1}$, respectively. All runs follow the same framework. Star formation follows the Springel & Hernquist model Springel & Hernquist (2003). Stars are formed stochastically after gas reaches the density threshold of $n = 0.1 \text{ Hcm}^{-3}$. The formation process obeys the Kennicutt-Schmidt relation (Kennicutt Jr 1998) and Chabrier (2003) initial mass function. Stars evolve and feed back the mass to the interstellar medium via Type Ia and Type II supernovae. Presence of a redshift-dependent, spatially uniform, ionizing UV background radiation field cools metal-enriched gas. The radiation field of nearby AGN activities further adjust the cooling process by superimposing it with the UV background. When a halo is sufficiently massive, a super massive black hole (SMBH) forms, accretes gas from the nearby area and contributes energy back into its surroundings. For a more comprehensive understanding of IllustrisTNG, we direct the reader to the work of Pillepich et al. (2017).

The merger trees were constructed by directly tracking the baryonic content of the subhalos Rodriguez-Gomez et al. (2015). They were later used to create a dataset of merging galaxies by Margalef-Bentabol et al. (2024). They selected galaxies from TNG100 and TNG300. The dataset consists of galaxies in the

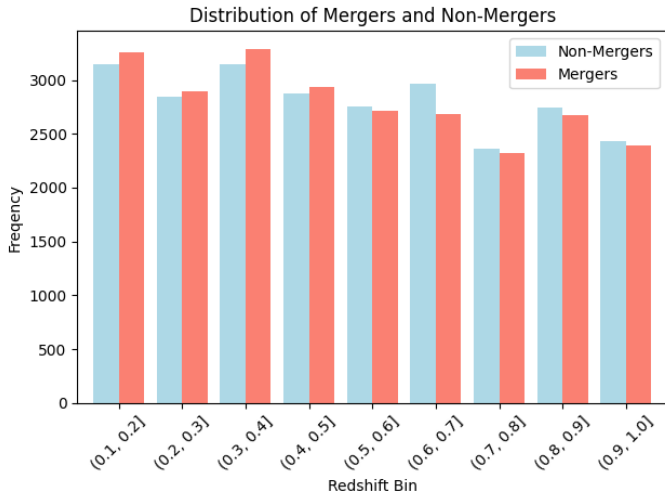


Fig. 1. Distribution of galaxies across redshifts. Y axis shows number of galaxies in each redshift bin and X axis redshift bin.

redshift range [0.1, 1.0). Merging galaxies either had a merger event in the past 0.3 Gyr or will have one in the next 0.8 Gyr. Margalef-Bentabol et al. (2024) only consider major mergers where the stellar mass ratios are greater than 4:1. Additionally, they categorize mergers that are 0.8 to 0.1 Gyr before coalescence as pre-mergers, 0.1 Gyr before to 0.1 Gyr after as ongoing mergers, and 0.1 to 0.3 Gyr after the coalescence as post-mergers.

2.2. Mock images

Simulated galaxy images are then processed to mimic HSC observations as described in Margalef-Bentabol et al. (2024). The sum of spectral energy distribution of all stellar particles in the image is passed through the filter to create a projected 2D map. Then each image is convolved with HSC i-band PSF. On top of that, Poisson noise that occurs in optical devices is added, and the image is injected into cutouts of real HSC observations. For a more complete description of how the synthetic images were generated, we direct the reader to (Rodriguez-Gomez et al. 2019). A physical size of the images was set to 160 kpc as it is approximately the typical separation between binary mergers based on simulations (Qu et al. 2017; Moreno et al. 2019). Images are 320x320, 192x192, 160x160, and 128x128 pixels for [0.1, 0.31), [0.31, 0.52), [0.52, 0.76), and [0.76, 1.0) redshift bins respectively. We randomly divided the images into three sets in the 75:15:10 ratio. The training set, used to fit the parameters, the validation set, providing an evaluation of a model while tuning the model’s hyperparameters, and finally the test set, used for an unbiased evaluation of the final model. Galaxies were divided, so that galaxies belonging to the same merger sequence are included in only one of the three sets. The distribution of galaxies across redshifts can be seen in Fig. 1, and the distribution of galaxies across merging times in Fig. 2.

3. Methodology

3.1. Sérsic profile fitting

We used statmorph (Rodriguez-Gomez et al. 2019) – an open source Python package for calculating morphologies of galaxy images to fit 2D Sérsic profile of each galaxy in the image. First,

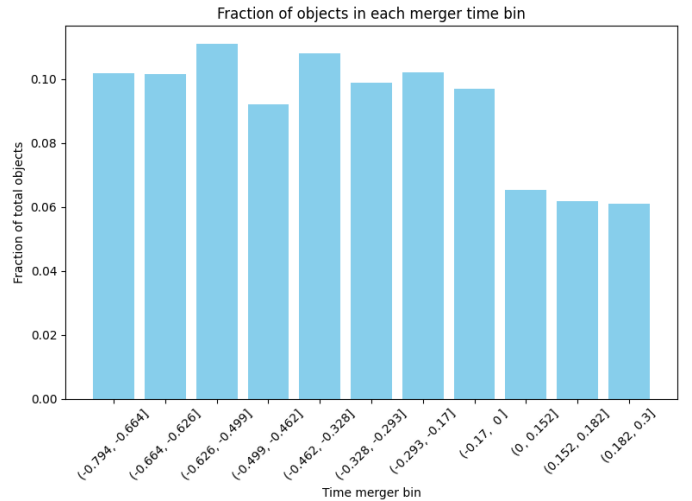


Fig. 2. Distribution of galaxies across pre-merging times and post-merging times. Y axis shows fraction of galaxies and X axis merging time bin in Gyr.

we create a segmentation map using the SEP Python package - code derived from the Source Extractor (Bertin & Arnouts 1996) code base. A segmentation map is a map the same size as the original image in which every pixel has an assigned label such that pixels with the same label belong to the same source, and defines the area over which morphological parameters are calculated. Since each pixel value is a combination of background and light from objects, SEP estimates the background level at every point in the image and subtracts it from the original image to accurately measure the flux of the objects. With background-subtracted data SEP performs object detection. We set the detection threshold to a value of 1.5σ where σ is the global background root mean square and minimum number of pixels required for an object is set to 5. Then overlapping but different sources are separated using a deblending algorithm to isolate the galaxy of interest for calculations.

For each galaxy in the image we perform photometric measurements and estimate the Sérsic parameters (half light radius, surface brightness at half-light radius, Sérsic index, position of the center of the galaxy, ellipticity of the profile, and rotation angle). The estimated Sérsic parameters serve as an initial guess for the Sérsic parameters used to create model images of the galaxies. Providing good initial guesses is crucial because the Levenberg–Marquardt algorithm (Geda et al. 2022) used for fitting is sensitive to initial parameters and, if provided with bad initial guesses, it may return parameters that correspond to a local minimum.

Sérsic profiles of each galaxy in every image were subtracted from the original image, creating a residual image, and cropped to 128 x 128 pixels. Resizing the image is done after subtraction of Sérsic profiles from original sized image to ensure the good quality of the residuals on the edges of the images. The steps used to create training datasets are shown in Fig. 3. Examples of non-merging and merging galaxies in the dataset are shown in Fig. 4.

3.2. Deep learning

3.2.1. Convolutional Neural Network

A neural network consists of an input layer, multiple hidden layers, and an output layer. The input is processed through a se-

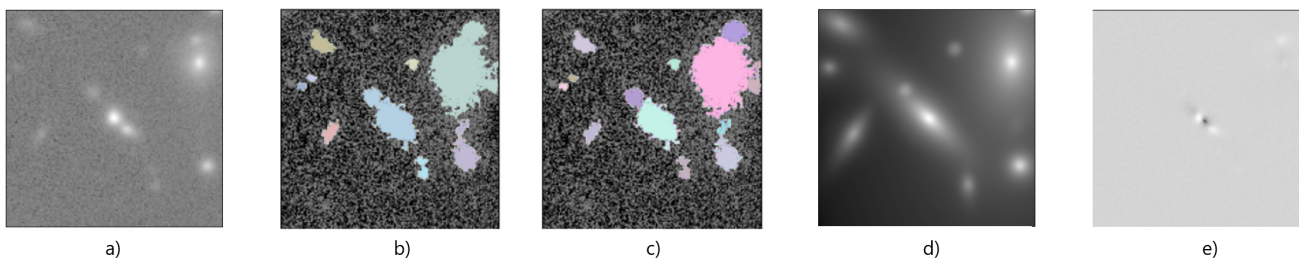


Fig. 3. Preprocessing steps. a) Original image, b) we create segmentation map, and c) deblend it to isolate overlapping galaxies. d) we fit Sérsic profile to each galaxy in the image. e) we subtract Sérsic profiles from the original image to create the residual image.

ries of calculations in hidden layers. A convolutional neural network (CNN) introduces convolutional layers comprised of learnable filters that convolve across the input image producing feature maps (FM) that capture spatial features. Convolution as an element-wise multiplication is always a linear transformation. To avoid reducing the problem to linear regression in order to learn more complex structures in the data, FMs are passed through an activation function that is nonlinear. Arguably the most common one, the rectified linear unit (ReLU; Nair & Hinton 2010) function, returns 0 if it receives any negative input, but for any positive input, it returns its value. A pooling layer is used to summarise features that lie in the close regions of a feature map, making the model invariant to changes in positions of features in the input image. It also down-samples the input image, so there are fewer parameters to learn during the training and reduces the computational effort of the process. Batch normalization layers rely on normalising the output of a hidden layer by rescaling and recentring it before feeding it as the input to the next one. A dropout technique causes some number of randomly chosen layer’s outputs to drop out, which means setting the output to 0 during training. It causes the network to never rely on activation of any specific neurons but forces it to learn additional information and helps preventing overfitting.

3.2.2. Training and architecture

The raw images, model images, and residual images are linearly normalized in a range of 0 to 1. These preprocessed images serve as input for all three CNNs. Each image is processed through a series of three convolutional layers, using 128 kernels of sizes 13×13 , 11×11 , and 9×9 . After each convolutional layer, the ReLU activation function is applied, followed by batch normalization, a 20% dropout, and 2×2 max pooling. After the four convolutional layers, the output is flattened and passed to two fully connected layers with 512 and 128 neurons, respectively. In these layers, every neuron is connected to all the outputs from the preceding layer. After each fully connected layer, activation, batch normalization, and 20% dropout are applied again. The output of the network is a single neuron activated by a softmax function that provides values representing the likelihood that the image contains a merger. The loss of the network was determined using the binary cross-entropy function and was optimized with the ADAM (Diederik 2014) algorithm with learning rate $\alpha = 3 \cdot 10^{-4}$. The CNN has 8 186 113 total trainable parameters. All networks were trained for 50 epochs. All three networks showed signs of overfitting after around 15 epochs, where training accuracy kept increasing while validation accuracy remained relatively still. It means that the problem does not take longer than 50 epochs to train. We used the set of tuned weights and

biases for the epoch that provided the highest value of validation accuracy before showing signs of overfitting for classification for the threshold for which precision is equal to recall. A summary of data pipeline from the creation of the data to the training of the model is shown in Fig. 5.

3.2.3. Evaluation metrics

In binary classification problems, a model can correctly or incorrectly assign a class for a given input. True positive (TP) is an object of positive label (merger) that is correctly classified, and true negative (TN) is an object of negative label (non-merger) that is correctly classified. Similarly, a false positive (FP) is an image of the actual negative label classified as positive and false negative (FN) and vice versa. To evaluate an already trained model, we use several metrics such as accuracy, precision, F1 score, and receiver operating characteristic curve (ROC-curve).

Accuracy is the number of correct predictions divided by the total number of predictions:

$$\text{Accuracy} = \frac{TP + TN}{TP + TN + FP + FN} .$$

Precision is the number of correctly identified positive cases divided by the total number of predicted positive cases,

$$\text{Precision} = \frac{TP}{TP + FP} .$$

Recall is equal to the number of correctly predicted positive cases divided by the total number of true positive cases,

$$\text{Recall} = \frac{TP}{TP + FN} .$$

The F-1 score is the harmonic mean of the precision and the Recall:

$$\text{F-1} = \frac{2}{\text{Precision}^{-1} + \text{Recall}^{-1}} .$$

The last metric used is the area under the curve (AUC). The receiver operating characteristic curve (ROC) shows True Positive Rate (TPR) against False Positive Rate (FPR) at different decision thresholds. TPR is the proportion of actual positive cases correctly identified by the model, while the FPR is the proportion of actual negative cases incorrectly identified as positive. AUC is the area under this curve and ranges in value from zero to one. A model whose predictions are always wrong has an AUC of 0 and a model whose predictions are always correct has an AUC of 1. For a random classifier, $\text{AUC} = 0.5$, ROC is a diagonal line and a model has no capacity to distinguish between positive and negative class.

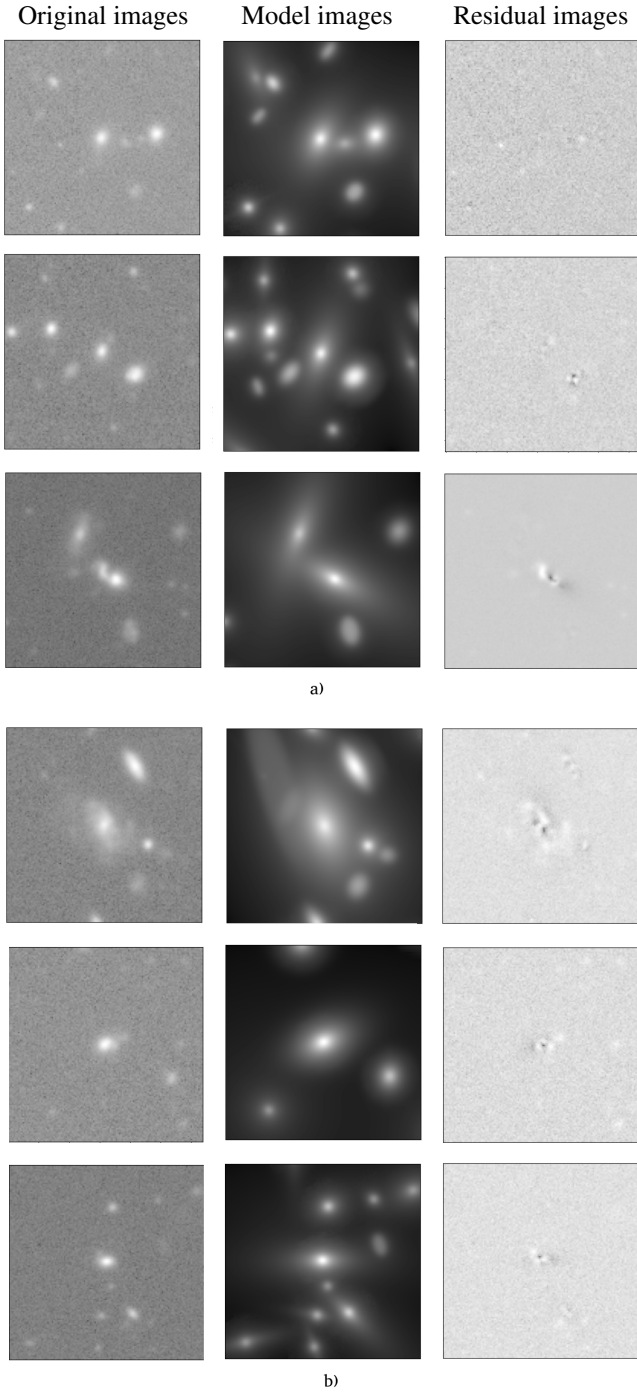


Fig. 4. Examples of mergers (a) and non-mergers (b) used for training. Left column: original images. Middle column: fitted Sérsic profiles. Right column: images after subtraction of Sérsic profiles. A power-law normalization with exponent 0.2 was used to display the images.

4. Results

We show the performance of all three networks using the evaluation metrics described in Sect. 3. Evaluation metrics scores depend on the choice of a decision threshold as it changes the required score to classify galaxy as a merger. Here, we set the threshold for each CNN independently, but the change in metrics as a function of threshold was also examined in Fig. 6. For all CNNs, we choose the decision threshold at which precision equals recall to achieve a balanced trade-off

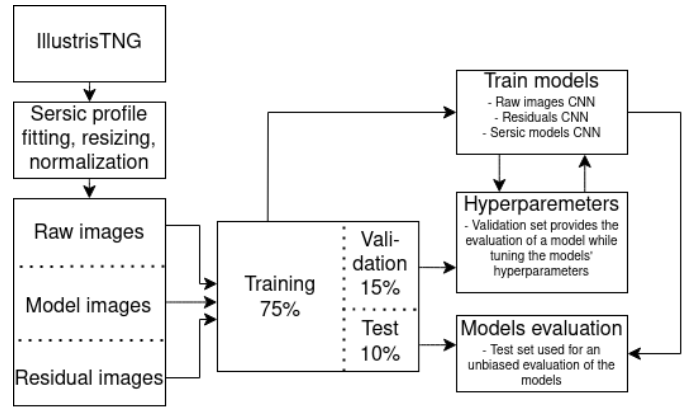


Fig. 5. Data pipeline summary. Three datasets were created - raw images, Sérsic profiles images and residual images. Images were cropped to 128 x 128 pixels, linearly normalized, and divided in 75:15:10 ratio into the training set, the validation set, and the test set.

between the rate of correctly identified positives and the rate of false positives, as both false positives and false negatives are equally undesirable. For CNN1, CNN2, and CNN3 it is 0.39, 0.47, and 0.49 respectively. CNN1 and CNN2 achieve their peak accuracy for these thresholds. The decline in accuracy after the peak is slower for CNN3 than CNN1 and CNN2.

The overall performance across the entire redshift range for all networks is summarized in Table 1. The results show that the CNN1 performs the best in terms of accuracy - 74%. CNN2 and CNN3 have similar overall accuracy - correctly classifying about, respectively, 70% and 68% of all images.

We check how the performance of all models changes as a function of redshift in Fig. 7, and across merging time bins in Fig. 8. We performed bootstrapping (Efron 1979), a resampling technique, in which multiple new samples (in our case 1000 resamples for each bin) are drawn with replacement from the original data to estimate uncertainties. All three networks show similar behavior across the redshift bins. As expected, the accuracy gradually decreases with redshift due to the deterioration of spatial resolution at higher redshifts, with the exception of the first redshift bins, where we observe an increase in accuracy for redshifts 0.1 to 0.3 for CNN1 and CNN3, and for redshifts 0.1 to 0.4 for CNN2. This is most likely because these images were originally larger (320x320 pixels) and resized to 128x128, potentially causing some loss of information. As seen by the higher fraction of correctly identified mergers, CNN1 classifies mergers best in almost all merging stages (-0.79 Gyr to 0.18 Gyr). CNN3 classifies mergers with similar precision as CNN1 in the latest stage of the merging process (0.18 to 0.3 Gyr). As summarized in Table 2, CNN1 correctly classifies $79.3 \pm 0.6\%$ of pre-mergers and $58.8 \pm 1.5\%$ of post-mergers, CNN2 correctly classifies $76.6 \pm 0.6\%$ of pre-mergers and $53.4 \pm 1.6\%$ of post-mergers, and CNN3 correctly classifies $73.3 \pm 0.6\%$ of pre-mergers and $55.5 \pm 1.4\%$ of post-mergers. Reported values are the mean fractions of correctly classified post-mergers and pre-mergers for each model, with the error represented as the difference between the mean and the upper bound of the 95% confidence interval of 1000 bootstrap resamples.

As shown in Fig.9, the distribution of Sérsic profile ellipticity for mergers and non-mergers is different. There are more

Table 1. Overall performance of CNN1 (raw images network), CNN2 (Sérsic profiles network) and CNN3 (residual images network).

Method	Accuracy	Precision	Recall	F1
CNN1	74%	73%	74%	74%
CNN2	70%	70%	70%	70%
CNN3	68%	68%	69%	68%

Table 2. Fraction of correctly classified pre-mergers and post-mergers for all CNNs.

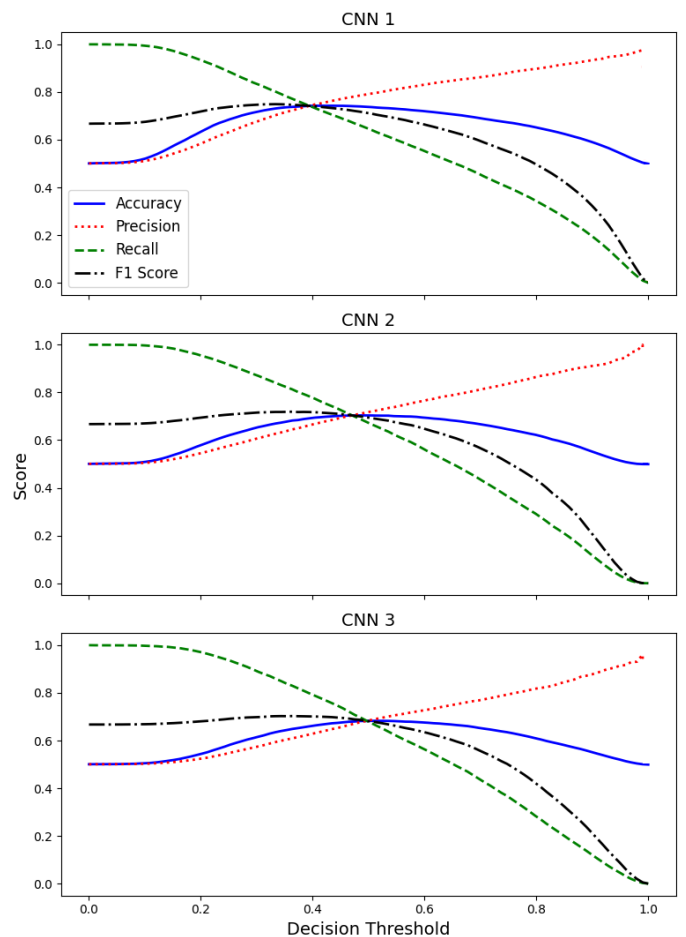
Method	Frac. pre-mergers	Frac. post-mergers
CNN1	79.3 ± 0.6%	58.8 ± 1.5%
CNN2	76.6 ± 0.6%	53.4 ± 1.6%
CNN3	73.3 ± 0.6%	55.5 ± 1.4%

non-mergers with low ellipticity than mergers. Statistically, mergers will have a more elliptical profile shape because they have undergone processes that could potentially distort their shape. Studying the dependence of metric values on the Sérsic profile shape will help us to understand to what extent the shape of a galaxy is useful in the evaluation of the network. The metrics for each Sérsic ellipticity bin are shown in Fig.10. We observe a high accuracy for low ellipticities across all networks, which then decreases and increases again around the bin (0.65, 0.7]. Precision decreases in the first three bins, then increases, reaching its maximum in the same bin. This results from the fact that the metrics are sensitive to class imbalance within a given bin. Higher ellipticities contain more mergers than non-mergers, so naturally, the number of TPs increases with the bin, while the number of FPs decreases. To mitigate the impact of this imbalance, the number of mergers and non-mergers was set equal in each bin. Each bin contains 500 mergers and 500 non-mergers. If the number of mergers or non-mergers in a bin is less than 500, the number of the less frequent type of galaxy is selected for that bin. Galaxies are randomly selected for each bin 20 times. Fig.11 shows the average metrics along with their standard deviations. As a result, we now observe a significantly greater ability of all networks to recognize mergers at low ellipticities than at high ellipticities, as indicated by the higher precision and only slightly decreasing accuracy, which decreases significantly only for CNN3 at the highest ellipticities. ROCs of all CNNs are shown in Fig. 12, and confusion matrices in Fig. 13. The overall best network is CNN1, followed by CNN2, and CNN3. CNN1 performs better in recognizing merging galaxies. 74.5% of them are correctly identified, while for non-merging galaxies, this number drops to 73.7%. CNN2 and CNN3 show similar performance. CNN2 correctly predicts 70.5% of mergers and 70.3% of non-mergers, while CNN3 correctly predicts 69.1% of mergers and 67.3% of non-mergers.

5. Discussion

5.1. CNNs comparison

CNN1 achieves the highest overall accuracy of 74%, outperforming the other two networks in classifying both mergers and non-mergers. Source position and shape information appear to be slightly more important for distinguishing between mergers and non-mergers, as CNN2 achieves somewhat better performance (70%) in terms of accuracy than CNN3 (68%). This shows that the lack of source position and shape information and the absence of double nuclei features during training—features

**Fig. 6.** Performance metrics as a function of threshold of CNN1 (top panel), CNN2 (middle panel), and CNN3 (lower panel). Accuracy is shown with blue solid line. Precision with red dotted line. Recall with green dashed line, and F1 with black dashed dotted line.

that could be removed through Sérsic profile subtraction—can confuse the network and reduce its ability to distinguish between mergers and non-mergers to the same extent as the lack of residual information.

CNN1 was able to predict 79% of pre-mergers correctly, a score similar to CNN2, which achieved 77% accuracy in this task, and much higher than CNN3, which achieved 73% accuracy. This may suggest that source position and shape information is the most important factor in classifying pre-mergers. This would be expected because the CNNs are looking for galaxies close to the primary galaxy, and a lack of its presence strongly suggests there is no pre-merger event. However, it does not suggest that there is no post-merger event. We would expect the precision to increase gradually with pre-merging time, reaching its maximum around the merging event. This happens for CNN1 and CNN3 up to 0.17 Gyr before the merging event and up to 0.29 Gyr before the merging event for CNN2.

Residual features are critical for classifying post-mergers. CNN2, which lacks residual information, has the lowest post-merger classification accuracy (53%), while CNN3, which uses only residual information, performs slightly better at 56%. CNN1, with access to all information, performs best with 59% accuracy. Over time, precision decreases for all networks as post-merger features fade. CNN3 consistently outperforms CNN2 across all post-merging times, suggesting that Sérsic profile subtraction helps detect fainter post-merger features. All three net-

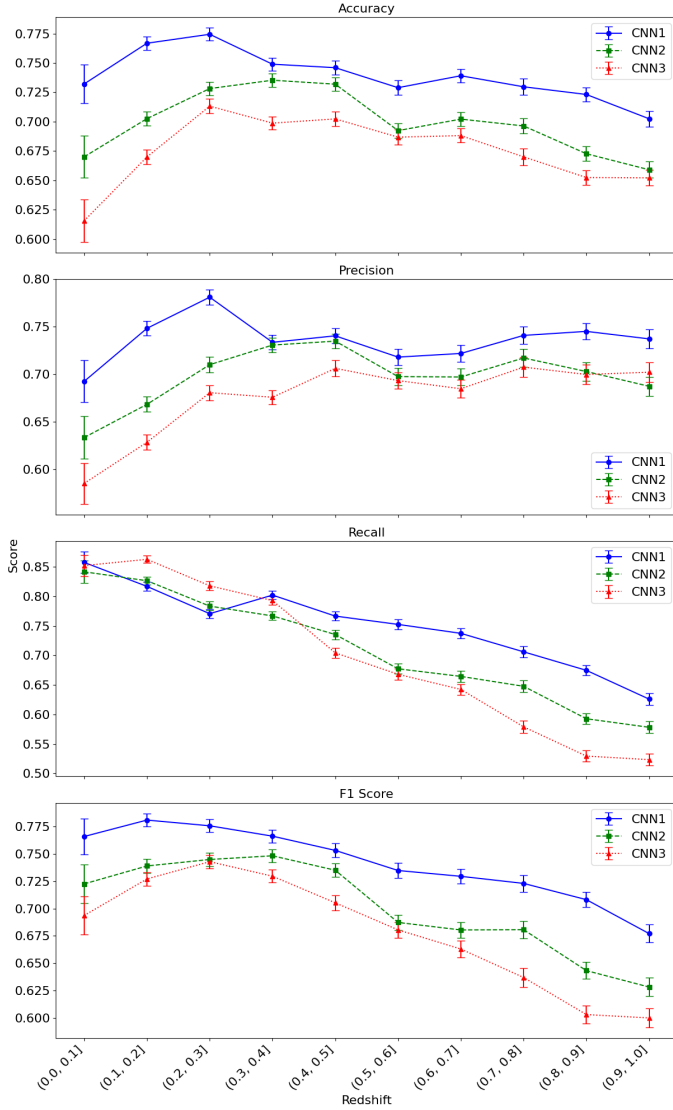


Fig. 7. Metric values across redshifts with standard deviation. From top to bottom: accuracy, precision, recall, and F1. Metrics for CNN1 are shown with blue solid line and circles, for CNN2 with green dashed line and squares, for CNN3 with red dotted line and triangle facing upwards.

works struggle more with distinguishing mergers from non-mergers in the post-merger stage than in pre-merger stages, possibly due to the faintness of residual features in post-merger galaxies. We can speculate that this is not due to the lack of double nuclei features or spatial information in general and also not due to the difference in the number of galaxies in each bin, as they are fairly similar for each pre- and post-merging stage as seen in Fig. 2. A potential reason for this is that the residual features in the post-merger stage may be fainter and more difficult to detect.

Mergers with lower Sérsic profile ellipticity are more frequently correctly classified than those with higher ellipticity, as shown in Fig. 11. This may be because merger-induced distortions are more prominent in galaxies with more symmetric profiles.

The results in terms of accuracy are consistent with Margalef-Bentabol et al. (2024), who conducted similar studies on the same datasets using different methods, achieving accuracies of 70.5%–77.7%. The study also demonstrates that post-mergers are more difficult to classify than pre-mergers.

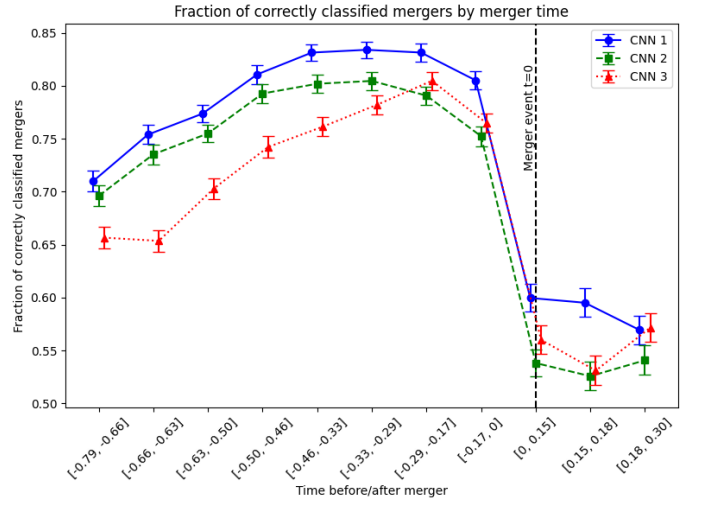


Fig. 8. Fractions of correctly classified mergers across merger times in Gyr with standard deviation. CNN1 is shown with blue solid line and circles. CNN2 with green dashed line and squares. CNN3 with red dotted line and triangles facing upwards.

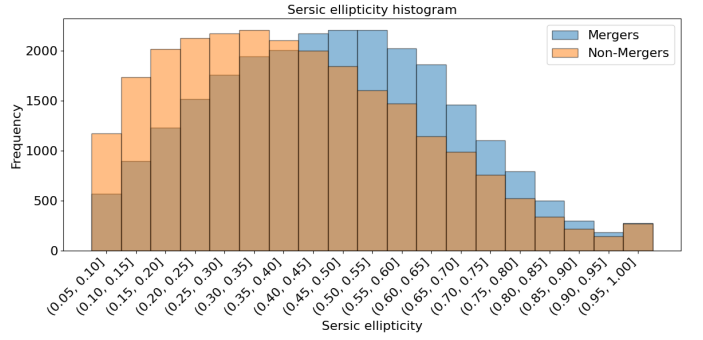


Fig. 9. Distribution of mergers and non-mergers across ellipticities of the Sérsic profile for the central galaxy. Y axis show the number of galaxies and X axis sérsic ellipticity bin.

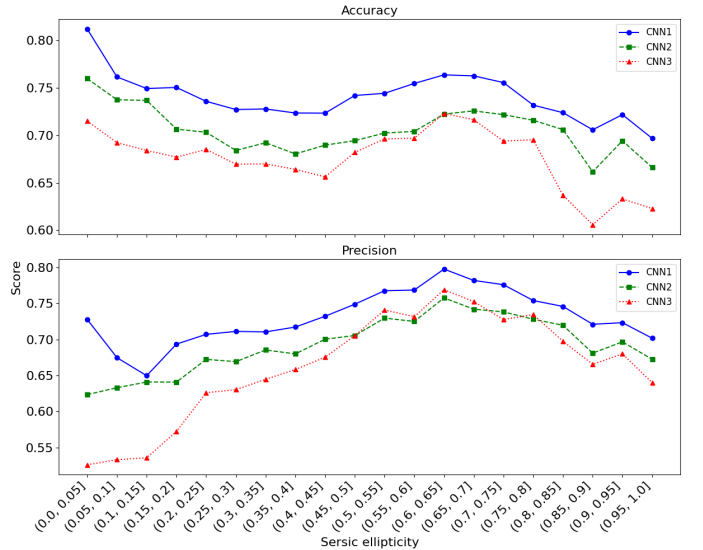


Fig. 10. Accuracy (top) and Precision (bottom) across Sérsic ellipticities. Metrics for CNN1 are shown with a blue solid line and circles, for CNN2 with green dashed line and squares, for CNN3 with red dotted line and triangle facing upwards.

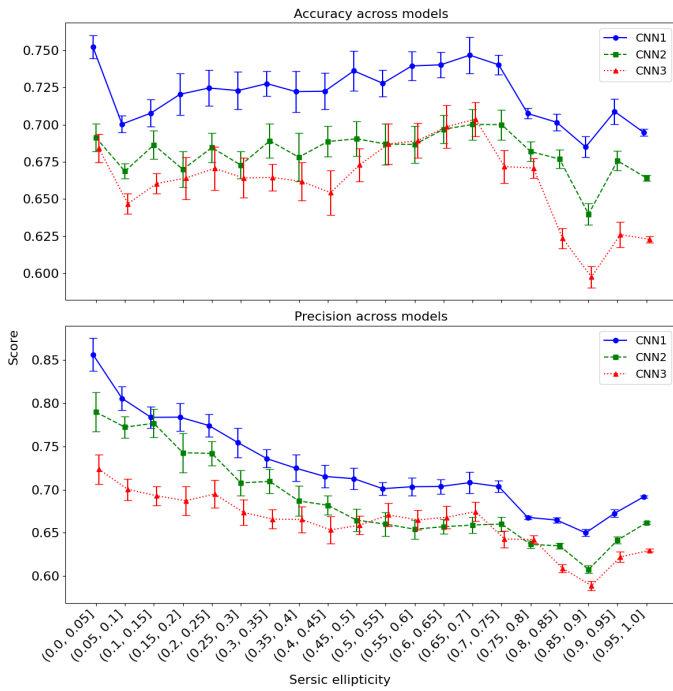


Fig. 11. Accuracy (top) and Precision (bottom) with standard deviation across Sérsic ellipticities for balanced bins. Each bin contains 500 mergers and 500 non-mergers. If the number of mergers or non-mergers in a bin is less than 500, the number of the less frequent type of galaxy is selected for that bin. Metrics for CNN1 are shown with a blue solid line and circles, for CNN2 with green dashed line and squares, for CNN3 with red dotted line and triangle facing upwards.

5.2. Occlusion

Following Pearson et al. (2022), occlusion experiments were performed on five mergers and five non-mergers. This technique is used to visualize what parts of the image are important for classification, as CNN feature maps are very unintuitive in deeper layers. In Fig. 14 we choose mergers that were: a) classified as mergers by all three CNNs, b) classified as non-mergers by all three CNNs, c) classified as mergers by CNN1 and as non-mergers by CNN2 and CNN3, d) classified as mergers by CNN2, and as non-mergers by CNN1 and CNN3, and e) classified as mergers by CNN3 and as non-mergers by CNN1 and CNN2. We also take non-mergers in Fig. 15 that were: a) classified as non-mergers by all three CNNs, b) classified as mergers by all three CNNs, c) classified as non-mergers by CNN1 and as mergers by CNN2 and CNN3, d) classified as non-mergers by CNN2, and as mergers by CNN1 and CNN3, and e) classified as non-mergers by CNN3 and as mergers by CNN1 and CNN2. The occlusion experiment relies on covering the image with a box (we used 8×8 pixels), evaluating it, shifting the box one pixel to the right so it covers different pixels, evaluating it again, and repeating it all over until the box reaches the lower right corner of an image. The occluded images are treated as normal galaxy images by a network. For CNN1 and CNN3 we used a box filled with noise with the properties of the image background, and for CNN2 we used a box filled with 0 values. This is done to not introduce structures that were not previously seen by the network, as there are no empty chunks in original images and residual images and there are no noise structures on the model images. This technique allows us to create an importance heatmap, which represents the average classification when each pixel was occluded. For mergers, important parts of the image will have lower scores

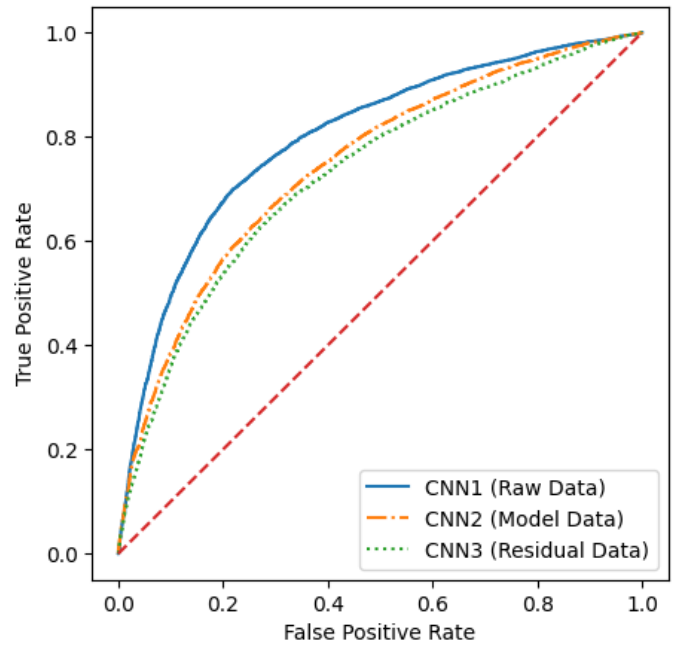


Fig. 12. ROC curves of all networks. This curve plots TPR against FPR at different classification thresholds. CNN1 is shown with blue solid line. CNN2 with yellow green dotted line, and CNN3 with dotted line. ROC curve of random classifier is depicted with diagonal, dashed, red line.

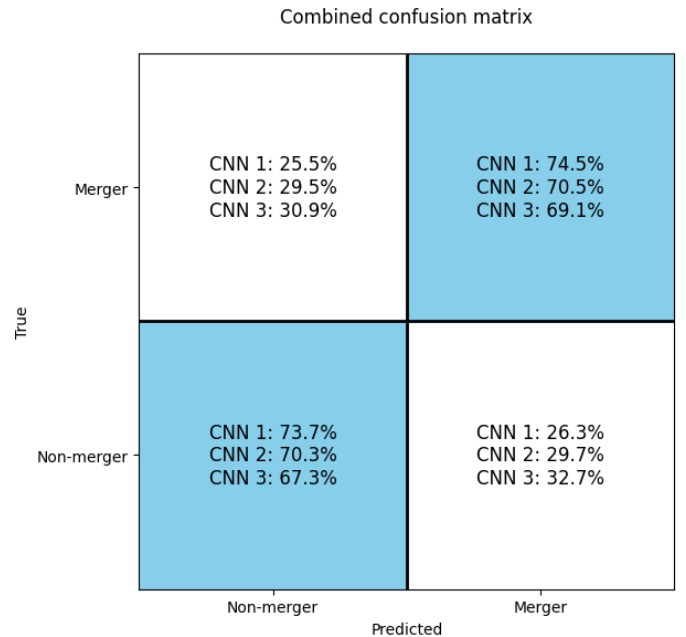


Fig. 13. Confusion matrix of all three CNNs normalized by row. This shows the proportion of predictions for each class.

in the importance heatmap than less important parts, and for non-mergers, important parts of the image will have higher scores than less important parts.

For selected known mergers (Fig. 14), CNN1 chooses the primary galaxy as the most important part of the image for classification (a), (c) and (d), as seen by the lowest prediction values in the place where the primary galaxy is. It can also be seen that the secondary galaxy plays a role in the classification score in

(b), though not that much as the outskirts of the primary galaxy. For selected known non-mergers (Fig. 15) we observe similar behavior. CNN1 also uses the primary galaxy to determine the classification for (a), (b), (c), and (d), where in (e) we see a shift of focus to the secondary galaxy, which in this case may be due to its greater brightness than primary galaxy. As expected, the most import region for classification of raw images seems to be the primary galaxy. This is the region where double nuclei are expected to be observed in merging galaxies, which are strong indicators of a merging process. This can also be seen in feature maps - convolutions of image with learnable kernel in Fig. 16, which confirms that double nuclei is probably one of the most important features for CNN1.

For selected known mergers (Fig.14) CNN2 is less influenced by the center galaxy than CNN1. The primary galaxy is the most important region for classification in (a), and (d), where in (b), (c), and (e) other galaxy models also contribute to the change of the score. For known non-mergers (Fig.15) CNN2 focuses on the primary galaxy only in (a). In (b), and in (d) it focuses on the outskirts of the primary galaxy. In (c) when it sees the secondary galaxy it changes its score in favor of a merger, and in (e) it focuses on the outskirts of both primary and secondary galaxy. For model images, the central region of the image also seems to be of the biggest importance for classification. Probably because the primary galaxy usually is the brightest in the image and the model network does not learn any additional information, just the shape and intensity of the model. In Fig. 14 (c) and in Fig. 15 (c) we see diminishing importance of the primary galaxy in favor of the secondary galaxy. This fact seems to support this idea, as it occurs when the size and intensity of both models are similar, and there is no single clearly dominating galaxy.

In the case of non-mergers (Fig. 15) CNN3 relies on the residual features more than for the merger case. This would agree with La Marca et al. (2024) who looked at the activation maps and for the non-mergers the most relevant parts of the images were also the features surrounding the primary galaxy. We can see that residual features play a role in evaluating the score on (b), (c), and (d), and (e). For known mergers (Fig.14) CNN3 looks into structures around the center, where the primary galaxy was located in (b), (d), and (e). In (a) and (c) it focuses on place where the secondary galaxy used to be. The residual network, as expected, focuses around the place where the primary galaxy used to be or its close surrounding. This has two explanations. Firstly - there can still be double nuclei features present as it may not follow the Sérsic profile and remains in the image, which is probably what happened in Fig. 14 (a) and (c) and Fig. 15 (b). Secondly - this is the region where faint merging features are expected to be present, and this can arguably be seen in Fig. 14 (e) and Fig. 15 (b), (d), and (e).

6. Conclusions

We trained three CNNs to perform merger vs non-merger classification using the IllustrisTNG simulation data with mock images that mimic the HSC survey: CNN1 on raw images, CNN2 on Sérsic models, and CNN3 on residual images. Then we evaluated the performance of all CNNs on the test data. CNN1 achieved the best accuracy of 74%.

It is possible to classify merging and non-merging galaxies using source position and shape information contained in Sérsic profiles with 70% accuracy (particularly pre-mergers with 77% precision), and using residual images with faint structures present in the image, achieving 68% accuracy (particularly post-mergers with 56% precision). Studying the results we draw

three important conclusions about the relative importance between spacial information and residual features for non-merger vs merger classification:

I. Both source position, shape information and residual features are crucial for non-merger vs merger classification.

- The almost equal overall performance of CNN2 and CNN3 indicates that both spatial and residual information are important for distinguishing between mergers and non-mergers. The lack of either type of information reduces the network's performance, as CNN1, which has access to all types of information, performs best in this task.
- The very good ability to recognize mergers at low ellipticities shows that, in addition to the source's position, its shape is also important for the network.

II. Source position and shape information is crucial for pre-merger classification

- Strong CNN1 and CNN2 performance compared to CNN3 in correctly classifying pre-mergers implies that source position and shape information is crucial for this task. The impact of its absence is observed in CNN3, which, lacking in relative position cues, performs significantly worse. Lack of a secondary galaxy near the primary galaxy strongly indicates a non-pre-merger event.

III. Residual features are crucial for post-merger classification.

- CNN2, devoid of residual context, performs the worst in classifying post-mergers, only 3% better than random pick. CNN1 having all information correctly predicts 59% of post-mergers. Introduction of residual features by subtracting Sérsic profiles drops the accuracy by 3% to 56% as seen in CNN3.
- The quality of the image can affect the network's ability to classify post-mergers. Higher-quality images may have more visible merging features in the residuals.

Future work will focus on evaluating networks on real HSC images labeled by the Galaxy Zoo project (Lintott et al. 2011). We will also apply the same data preprocessing method to the observations and train the networks. The differences between the performance of the simulation-trained network and the observations-trained network will be examined. New architectures will be tested to find the best way to learn both residual and spatial features.

Acknowledgments

We gratefully acknowledge Polish high-performance computing infrastructure PLGrid (HPC Center: ACK Cyfronet AGH) for providing computer facilities and support within computational grant no. PLG/2024/017417.

W.J.P has been supported by the Polish National Science Center project UMO-2023/51/D/ST9/00147.

A.P has been supported by the Polish National Science Center project UMO-2023/50/A/ST9/00579.

L.E. Suelves was supported by the Estonian Ministry of Education and Research (grant TK202), Estonian Research Council grant (PRG1006), and the European Union's Horizon Europe research and innovation programme (EXCOSM, grant No. 101159513).

B.M.B and L.W are supported by the project 'Clash of the Titans: deciphering the enigmatic role of cosmic collisions' (with project number VI.Vidi.193.113 of the research programme Vidi, which is (partly) financed by the Dutch Research Council (NWO)).

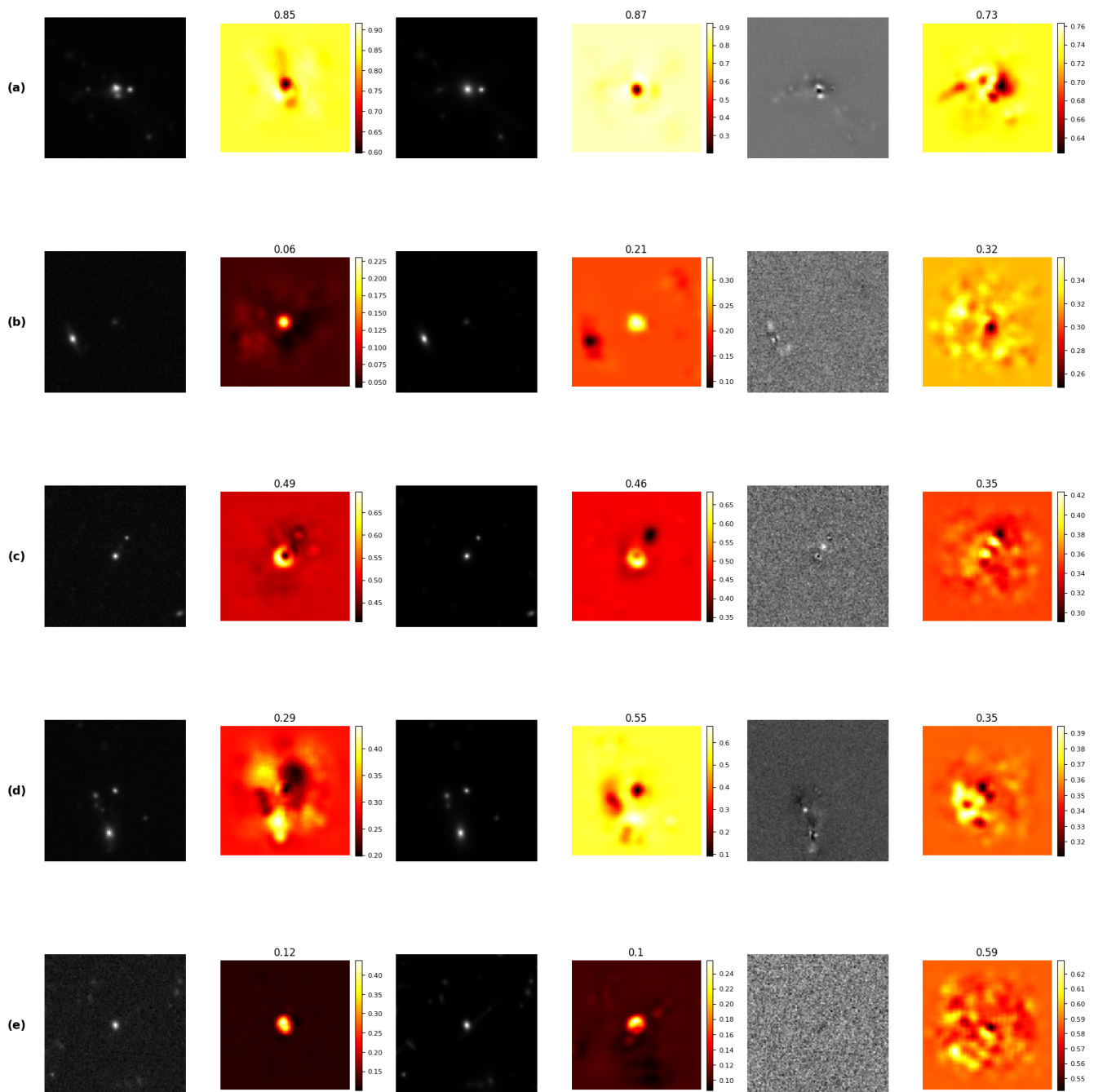


Fig. 14. Occlusion experiment for mergers that were: a) classified as mergers by all three CNNs, b) classified as non-mergers by all three CNNs, c) classified as mergers by CNN1 and as non-mergers by CNN2 and CNN3, d) classified as mergers by CNN2, and as non-mergers by CNN1 and CNN3, and e) classified as mergers by CNN3 and as non-mergers by CNN1 and CNN2. First two left columns show CNN1 input and corresponding heatmap. Two middle columns show CNN2 input and corresponding heatmap. Last middle columns show CNN3 input and corresponding heatmap. Above each heatmap there is a prediction for the original input, before performing occlusion experiment. Thresholds for CNN1, CNN2, and CNN3 are 0.39, 0.47, and 0.49 respectively.

References

- Abraham, R. G., Bergh, S. v. d., Glazebrook, K., et al. 1996, *The Astrophysical Journal*, Supplement series, Chicago, Vol. 107, no. 1 (Nov. 1996), p. 1-17
- Abraham, R. G., Van Den Bergh, S., & Nair, P. 2003, *The Astrophysical Journal*, 588, 218
- Ackermann, S., Schawinski, K., Zhang, C., Weigel, A. K., & Turp, M. D. 2018, *Monthly Notices of the Royal Astronomical Society*, 479, 415
- Alonso, M. S., Tissera, P. B., Coldwell, G., & Lambas, D. G. 2004, *Monthly Notices of the Royal Astronomical Society*, 352, 1081
- Barton, E. J., Geller, M. J., & Kenyon, S. J. 2000, *The Astrophysical Journal*, 530, 660
- Bershady, M. A., Jangren, A., & Conselice, C. J. 2000, *The Astrophysical Journal*, 119, 2645
- Bertin, E. & Arnouts, S. 1996, *A&AS*, 117, 393
- Bickley, R. W., Bottrell, C., Hani, M. H., et al. 2021, *Monthly Notices of the Royal Astronomical Society*, 504, 372
- Bournaud, F., Jog, C., & Combes, F. 2005, *Astronomy & Astrophysics*, 437, 69
- Chabrier, G. 2003, *Publications of the Astronomical Society of the Pacific*, 115, 763
- Ćiprijanović, A., Snyder, G. F., Nord, B., & Peek, J. E. 2020, *Astronomy and Computing*, 32, 100390
- Collaboration, P., Aghanim, N., Arnaud, M., et al. 2016, *Astronomy and Astrophysics*, 594, A13
- Conselice, C. J. 2003, *The Astrophysical Journal Supplement Series*, 147, 1

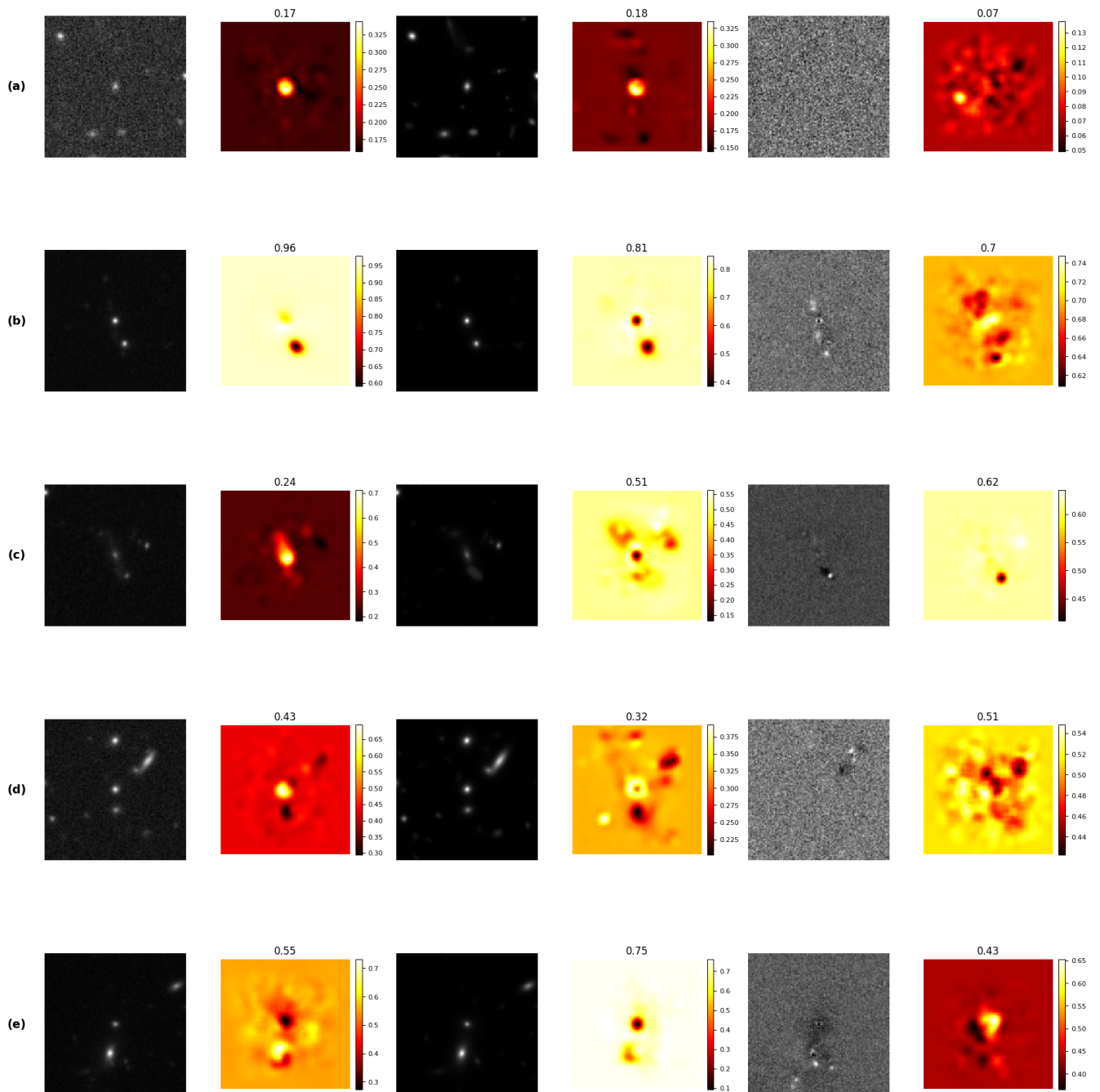


Fig. 15. Occlusion experiment for non-mergers that were: a) classified as non-mergers by all three CNNs, b) classified as mergers by all three CNNs, c) classified as non-mergers by CNN1 and as mergers by CNN2 and CNN3, d) classified as non-mergers by CNN2, and as mergers by CNN1 and CNN3, and e) classified as non-mergers by CNN3 and as mergers by CNN1 and CNN2. First two left columns show CNN1 input and corresponding heatmap. Two middle columns show CNN2 input and corresponding heatmap. Last two columns show CNN3 input and corresponding heatmap. Above each heatmap there is a prediction for the original input, before performing occlusion experiment. Thresholds for CNN1, CNN2, and CNN3 are 0.39, 0.47, and 0.49 respectively.

Conselice, C. J., Bershad, M. A., & Jangren, A. 2000, *The Astrophysical Journal*, 529, 886
Darg, D. W., Kaviraj, S., Lintott, C. J., et al. 2010, *Monthly Notices of the Royal Astronomical Society*, 401, 1043
De Propriis, R., Liske, J., Driver, S. P., Allen, P. D., & Cross, N. J. 2005, *The Astronomical Journal*, 130, 1516
Di Matteo, T., Springel, V., & Hernquist, L. 2005, *nature*, 433, 604
Diederik, P. K. 2014, (No Title)
Duncan, K., Conselice, C. J., Mundy, C., et al. 2019, *The Astrophysical Journal*, 876, 110
Efron, B. 1979, *The Annals of Statistics*, 7, 1
Ellison, S. L., Mendel, J. T., Patton, D. R., & Scudder, J. M. 2013, *Monthly Notices of the Royal Astronomical Society*, 435, 3627

Ferreira, L., Conselice, C. J., Duncan, K., et al. 2020, *The Astrophysical Journal*, 895, 115
Gao, F., Wang, L., Pearson, W., et al. 2020, *Astronomy & Astrophysics*, 637, A94
Geda, R., Crawford, S. M., Hunt, L., et al. 2022, *The Astronomical Journal*, 163, 202
Hildebrandt, H., Wolf, C., & Benítez, N. 2008, *Astronomy & Astrophysics*, 480, 703
Huertas-Company, M., Gravet, R., Cabrera-Vives, G., et al. 2015, *ApJS*, 221, 8
Ivezić, Ž., Kahn, S. M., Tyson, J. A., et al. 2019, *The Astrophysical Journal*, 873, 111
Kennicutt Jr, R. C. 1998, *The astrophysical journal*, 498, 541

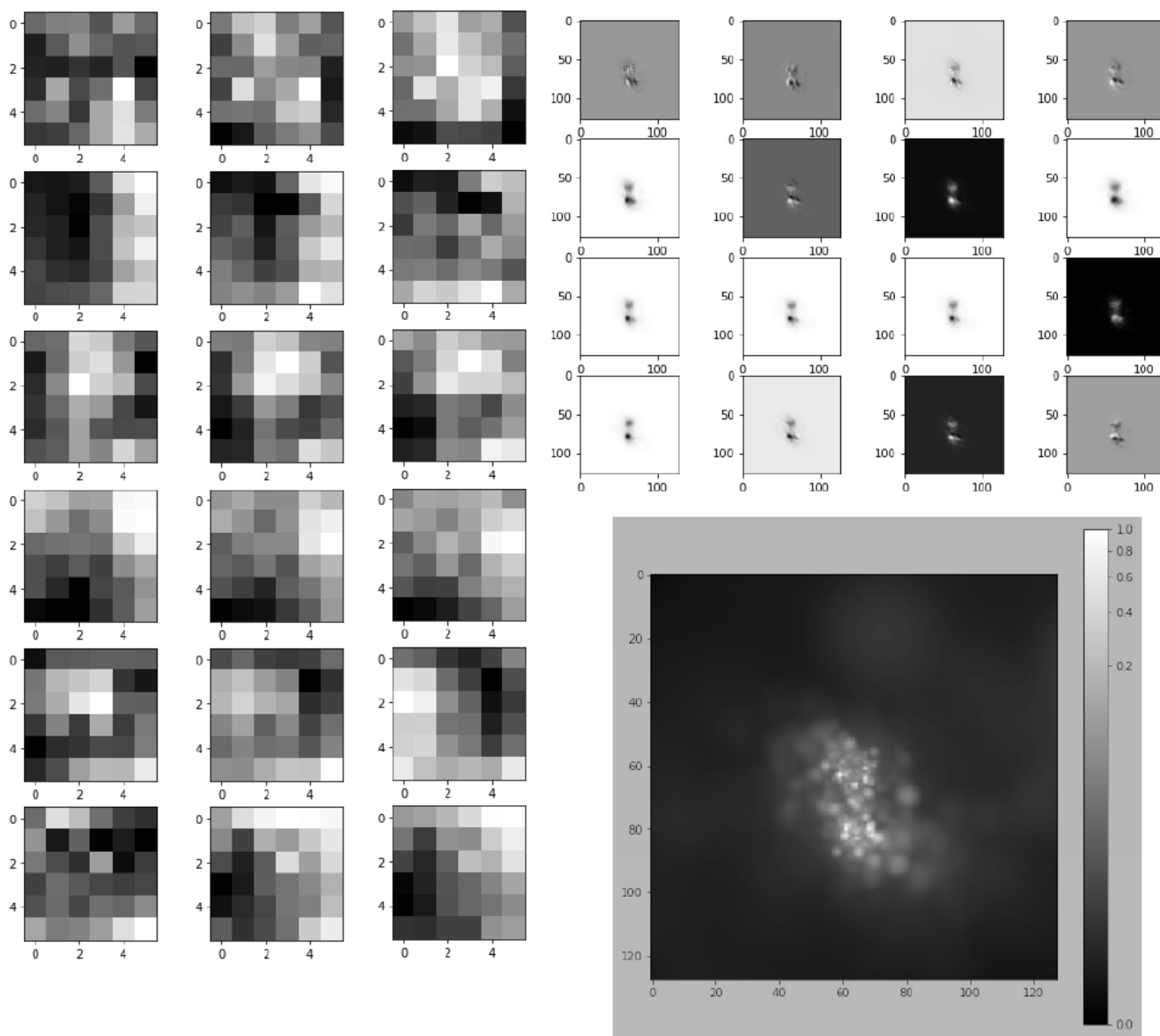


Fig. 16. Left half of the image: Learnable kernels of CNN1. Upper right quarter: feature maps - results of the convolutions of original image with kernels of CNN1. Lower right quarter: original image.

Kent, S. M. 1985, *Astrophysical Journal Supplement Series* (ISSN 0067-0049), vol. 59, Oct. 1985, p. 115-159., 59, 115
 La Marca, A., Margalef-Bentabol, B., Wang, L., et al. 2024, *Astronomy & Astrophysics*, 690, A326
 Lambrides, E. L., Watts, D. J., Chiaberge, M., et al. 2021, *The Astrophysical Journal*, 919, 43
 Laureijs, R., Amiaux, J., Arduini, S., et al. 2011, arXiv preprint arXiv:1110.3193
 Lin, L., Patton, D. R., Koo, D. C., et al. 2008, *The Astrophysical Journal*, 681, 232
 Lintott, C., Schawinski, K., Bamford, S., et al. 2011, *Monthly Notices of the Royal Astronomical Society*, 410, 166
 Lotz, J. M., Jonsson, P., Cox, T., & Primack, J. R. 2010, *Monthly Notices of the Royal Astronomical Society*, 404, 575
 Lotz, J. M., Primack, J., & Madau, P. 2004, *The Astronomical Journal*, 128, 163
 Mantha, K. B., McIntosh, D. H., Ciaschi, C. P., et al. 2019, *Monthly Notices of the Royal Astronomical Society*, 486, 2643
 Margalef-Bentabol, B., Wang, L., La Marca, A., et al. 2024, arXiv preprint arXiv:2403.15118
 Moreno, J., Torrey, P., Ellison, S. L., et al. 2019, *Monthly Notices of the Royal Astronomical Society*, 485, 1320
 Mundy, C. J., Conelice, C. J., Duncan, K. J., et al. 2017, *Monthly Notices of the Royal Astronomical Society*, 470, 3507

Nair, V. & Hinton, G. E. 2010, in *Proceedings of the 27th international conference on machine learning (ICML-10)*, 807-814
 Nelson, D., Springel, V., Pillepich, A., et al. 2019, *Computational Astrophysics and Cosmology*, 6, 1
 Nevin, R., Blecha, L., Comerford, J., & Greene, J. 2019, *The Astrophysical Journal*, 872, 76
 Okamura, S., Kodaira, K., & Watanabe, M. 1984, *Astrophysical Journal, Part 1* (ISSN 0004-637X), vol. 280, May 1, 1984, p. 7-14., 280, 7
 Pearson, W., Suelves, L., Ho, S.-C., et al. 2022, *Astronomy & Astrophysics*, 661, A52
 Pearson, W., Wang, L., Alpaslan, M., et al. 2019a, *Astronomy & Astrophysics*, 631, A51
 Pearson, W., Wang, L., Trayford, J., Petrillo, C., & Van Der Tak, F. 2019b, *Astronomy & Astrophysics*, 626, A49
 Pillepich, A., Springel, V., Nelson, D., et al. 2017, *Monthly Notices of the Royal Astronomical Society*, 473, 4077
 Qu, Y., Helly, J. C., Bower, R. G., et al. 2017, *Monthly Notices of the Royal Astronomical Society*, 464, 1659
 Rodriguez-Gomez, V., Genel, S., Vogelsberger, M., et al. 2015, *Monthly Notices of the Royal Astronomical Society*, 449, 49
 Rodriguez-Gomez, V., Snyder, G. F., Lotz, J. M., et al. 2019, *Monthly Notices of the Royal Astronomical Society*, 483, 4140

- Sánchez, H. D., Martín, G., Damjanov, I., et al. 2023, *Monthly Notices of the Royal Astronomical Society*, 521, 3861
- Snyder, G. F., Lotz, J., Moody, C., et al. 2015, *Monthly Notices of the Royal Astronomical Society*, 451, 4290
- Springel, V. & Hernquist, L. 2003, *Monthly Notices of the Royal Astronomical Society*, 339, 289
- Suelves, L., Pearson, W., & Pollo, A. 2023, *Astronomy & Astrophysics*, 669, A141
- Takamiya, M. 1999, *The Astrophysical Journal Supplement Series*, 122, 109
- Tasca, L., Le Fèvre, O., López-Sanjuan, C., et al. 2014, *Astronomy & Astrophysics*, 565, A10
- Toomre, A. & Toomre, J. 1972, *Astrophysical Journal*, Vol. 178, pp. 623-666 (1972), 178, 623
- Ventou, E., Contini, T., Bouché, N., et al. 2019, *Astronomy & Astrophysics*, 631, A87
- Vogelsberger, M., Genel, S., Springel, V., et al. 2014, *Monthly Notices of the Royal Astronomical Society*, 444, 1518
- Walmsley, M., Ferguson, A. M., Mann, R. G., & Lintott, C. J. 2019, *Monthly Notices of the Royal Astronomical Society*, 483, 2968
- Wang, L., Pearson, W., & Rodríguez-Gomez, V. 2020, *Astronomy & Astrophysics*, 644, A87